A computational measurement of cartilaginous endplate structure using ultrashort time-to-echo MRI scanning

Ri-Chu Jin, Yong-Can Huang, Keith D.K. Luk, Yong Hu*

Department of Orthopaedics and Traumatology, The University of Hong Kong, Hong Kong SAR, P. R. China

***Corresponding Author:**

Dr. Yong Hu
12 Sandy Bay Road, Hong Kong
Duchess of Kent Children's Hospital
Department of Orthopaedic Surgery,
The University of Hong Kong
Pokfulam, Hong Kong
Tel: (852) 29740359
Fax: (852) 29740335
E-mail: yhud@hku.hk

Abstract

Background and Objective: Ultrashort time-to-echo (UTE) MRI scanning has been applied to observe the cartilaginous endplate (CEP) in intervertebral disc. CEP plays a critical role in IVD health and disease. Nevertheless, current measurements of CEP based on UTE MRI technique are still by manual segmentation, and observation of signal abnormality was usually time-consuming and often disturbed by subjective bias. This study hence proposed an efficient way to harvest the global parameters of CEP after UTE MRI scanning.

Methods: E*x-vivo* UTE-MRI scanning was performed using 12 goat lumbar spine specimens. After the UTE-MRI data were collected, the computational method for CEP segmentation and assessment was developed. Global view of CEP, e.g., surface morphology as well as distributions of thickness and signal intensity, were measured. Histological staining of the CEP as well as manual CEP segmentation was then conducted to validate the accuracy.

Results: Segmentation of CEP by the proposed method presented a good agreement with manual measurement, with mean Jaccard index of 0.7296 and mean Cohen's Kappa coefficient of 0.8286. The processing time for CEP segmentation and property measurements was 59.2 s which was much shorter than the manual measurement.

Conclusions: This newly-developed technique is able to qualitatively and quantitatively assess the CEP structure, which is very valuable for the clinicians and researchers to accurately evaluate the endplate health after UTE MRI scanning.

Keywords: ultrashort time-to-echo; MRI; intervertebral disc; cartilaginous endplate; image segmentation

1. Introduction

Intervertebral disc (IVD) degeneration is one of the most common musculoskeletal disorders, and it has been considered as one possible cause of low back pain. In the IVD, cartilaginous endplate (CEP) is a thin layer of hyaline cartilage positioned between the bony endplate and nucleus pulposus [1]. It prevents the bulging of the nucleus pulposus into the neighboring vertebral bodies and disperses the compressive loading experienced by the vertebra-disc complex [2]. Importantly, CEP acts as a selectively permeable barrier for nutrient transport into the intervertebral disc (IVD) in which most of the cells are nourished by this pathway [3]. The physiopathological changes in the CEP would result in an alteration of nutrient supply, in turn causing IVD degeneration [3]. Thus, CEP plays a key role in maintaining the health and function of IVD.

Using conventional MRI images, CEP is invisible due to very short T2 values (less than 1 msec) of its components [4]. This situation was not changed until some pulse sequences with the ability to detect short T2 components (as low as 8 μsec), *e.g.*, ultrashort time-to-echo (UTE), were developed [5-7]. After UTE MRI imaging, CEP was characterized as high intensity lines [7-11]. Additionally, abnormal patterns such as the focal loss and irregularity of the line can be evaluated to assess CEP integrity in IVD degeneration [8, 9]. Interestingly, the thickness of CEP was measured by Moon and co-authors based on MRI images; they calculated the thickness of CEP line at five locations across sagittal section and then described thickness distribution of human CEP [7]. Nevertheless, this distribution only revealed the CEP thickness along one direction and failed to offer a global view. A spatial map to show comprehensive information of CEP MRI signal was also generated by a manually selected region of interest (ROI) in each

sagittal MRI image [11]. But this manual measurement procedure would be time consuming and easily disturbed by subjective bias.

For better structural assessment, a technique was hence developed based on the UTE-MRI images obtained from the goat lumbar spine. The goat lumbar IVD was used because it has similar structure and geometry as the human IVD [12]. In this work, an automatic algorithm was firstly used for CEP line segmentation in each sagittal UTE-MRI image; then all the CEP lines were assembled to obtain a global view of CEP. Subsequently, the structural properties, *i.e.*, morphology, thickness distribution and signal intensity distribution, could be evaluated both qualitatively and quantitatively. In all, a comprehensive quantitative assessment of CEP could be achieved in an objective and time saving way based on UTE-MRI imaging using this technique.

2. Methodology

2.1 Materials

A total of 12 lumbar spines from male goats between 6 and 9 months weighing between 17.5 and 25 kg were used in this study. The goats were sacrificed and the spinal columns from L2 to L6 were harvested *en bloc* for MRI scanning. This study was approved by the Committee on the Use of Live Animals in Teaching & Research, the University of Hong Kong (CULATR1872-09).

2.2 *Ex-vivo* MRI

*Ex-viv*o MRI scanning was executed on a Philips Achieva 3.0T scanner (PHILIPS,

Netherlands) with a body coil excitation and a phased-array coil reception. The scanned region contained goat's spine from L2 to L6. A 3-D UTE Shifting TE phase-encoded stack of spirals trajectory was employed [13], with scanning parameters as: FOV = 100×100×42 mm^3, TR = 6.90 ms, TE = 0.14 ms, acquisition voxel size = 0.4032×0.4032×1.2 mm^3, reconstructed voxel size = 0.2976×0.2976×1.2 mm^3 and scan time = 4 min 21 s.

2.3 Enhancement of CEP assessment based on MRI images

In this study, a method for CEP segmentation from UTE MRI images was proposed to facilitate 3D information acquisition and quantitative analysis. The method included three major procedures (Fig. 1): image preprocessing (*i.e.*, to prepare for the following CEP segmentation procedure by removing complex background, increasing image resolution and normalizing signal intensities), CEP segmentation (*i.e.*, to segment CEP lines from each sagittal UTE MRI image and get them assembled to obtain the entire CEP) and CEP property calculation (*i.e.*, to obtain global properties of CEP based on the segmented CEP).

(1) Image preprocessing

CEP signal is usually located in a complicated background in UTE MRI images, and these images are usually with limited image resolutions and various signal intensity ranges. These problems increase the difficulty of CEP segmentation, and image preprocessing procedure was hence developed to get them solved. ROI selection was first implemented to remove interference of the complicated background. A proper ROI should include signals of target IVD as well as its two neighboring CEPs but exclude other signals as many as possible. In each sagittal UTE MR image, ROIs could be selected manually or with an

automated method, such as the one introduced in Appendix A. After that block images were segmented from each sagittal UTE MRI image, and they were then up-sampled by zero-padding discrete cosine transform (DCT) for a higher resolution. Finally, these block images were normalized to a uniform signal intensity range between 0 and 255 for uniform parameter setting in the following procedures.

(2) CEP segmentation

After image preprocessing, a series of block images containing CEP information were obtained. CEP was revealed as a high-intensity line in each block image. In CEP segmentation procedure, these CEP lines were first segmented from block images and then assembled together to form the entire CEP.

CEP line could be segmented by determining its outer border (*i.e.*, the border far from IVD) and inner border (*i.e.*, the border close to IVD). Both of the borders had intersections with a line drawn in the block image along the Y direction. Along this Y-direction line, signal intensities corresponding to IVD and its two neighboring CEPs formed a "two-peak curve", and each peak of this curve corresponded to a CEP line. For each peak, the two intersections of CEP line borders and Y-direction line were located at its outer slope (*i.e.*, the slope far from the two-peak curve's bottom) and inner slope (*i.e.*, the slope close to the two-peak curve's bottom) respectively. These settings were illustrated in Fig. 2, and the strategy of CEP line segmentation could then be described as:

(1) Draw a Y-direction line at one X position;

(2) Recognize the two-peak curve;

(3) Locate the two intersections;

(4) Find another X position and repeat steps (1)-(3) unitl all X positions were attempted;

(5) Filter out valid intersections and form CEP line borders, and areas between the two borders were the segmented CEP line.

Specific steps for "two-peak curve" recognition and border intersection targeting can be found in Appendix B and C, respectively. In addition, an adjustable ratio coefficient γ_i was provided in this method to widen or narrow the segmented CEP line to meet the different definitions of CEP line in UTE MRI images in different studies. This adjustment process is also mentioned in Appendix C. All segmented CEP lines were then assembled to build the entire CEP. The positions of each CEP line should be matched with those in the original UTE MRI data during the assembling.

(3) CEP property calculation

Three CEP properties, *i.e.*, surface morphology, thickness distribution and UTE signal intensity distribution, were analyzed in this study.

Surface morphology can be visualized by topographic maps of inner and outer surfaces of CEP. Mean depth and cross sectional area are usually calculated for quantitative analysis [14, 15]. Mean depth is mean value of depths revealed by the surface topographic map. Cross sectional area is the area of the projection of the CEP surface topographic map to the cross sectional plane. CEP thickness is the shortest distance between the inner and outer surfaces. The thickness of one point on CEP surface was measured as the diameter of the

biggest sphere passing the point and located between inner and outer surfaces (i.e. the inscribed sphere), namely the length of AB in Fig. 3 (a). The thickness distribution map could be generated by projecting thickness distribution on CEP surface to a cross sectional plane (Fig. 3 (b)), similar as [16,17].

Similar as thickness distribution map, mean values of UTE signal intensities along the inscribed sphere diameter AB (Fig. 3 (a)) can be projected to a cross sectional plane as a distribution map [11].

2.4 Histological staining

After *ex-vivo* MRI scanning, the lumbar spine was fixed in 4% paraformaldehyde for 7 days, the discs at the level of L3/4 were separated, cut mid-sagittally, decalcified, dehydrated, embedded in paraffin wax, and finally cut into 5-μm-thick sections for hematoxylin and eosin (HE) and Masson-trichrome (MT) staining.

2.5 Data analysis

Twenty-four IVD samples with forty-eight CEP layers were scanned and analyzed in this study. To verify the reliability of CEP segmentation, results from the proposed algorithm were compared to a manual segmentation procedure conducted by a senior radiologist with 5 years experiences in MRI researches. The radiologist knew well about the display of CEP in UTE MRI images but knew little on the algorithm. The manual segmentation procedure was similar to the automatic segmentation. The radiologist manually drew the outer and inner borders of one CEP line and the area between the two borders were segmented. The

borders recognized by the radiologist have been pointed out by arrows in Fig. 4. In addition, manual segmentation was only conducted in the central part of IVD to decrease interference of annulus fibrosus, as shown in Fig. 4. The radiologist manually segmented CEP lines in the middle sagittal slices for each CEP. Then Jaccard index and Cohen's Kappa coefficient were calculated to examine the similarity between areas of these CEP lines and those of automatically segmented CEP lines. The computational time of varies processes was observed.

In addition, 20 CEP layers from 10 IVD samples had accepted histological staining after *ex-vivo* MRI scanning. Mean thicknesses of CEP lines revealed in HE and MT staining images were compared with corresponding CEP lines segmented from UTE MRI images with the proposed method. Pearson correlations and paired T tests were conducted.

3. Results

In the original sagittal UTE MRI image, one target IVD was selected as ROI (left image in Fig. 5 (a)). An IVD block image was segmented by the ROI (top right corner in Fig. 5 (a)). The resolution of block image was increased after the up-sampling process (bottom right corner in Fig. 5 (a)).

In the target block image, outer and inner border intersections of CEP lines were sequentially identified along X direction, forming the outer and inner borders, as is shown by the blue and green curves in Fig. 5 (b) respectively. A pair of outer and inner borders

determined a CEP line, as the green line shown in Fig. 5 (c). The entire CEP was then segmented by assembling all its corresponding CEP lines together. 3D visualization of the segmented CEPs adjacent to one target IVD was made by 3D slicer (v 4.4.0), as is shown in Fig. 5 (d). The segmented CEP lines can be confirmed by observing the histological images obtained after UTE scanning as the pink line shown in the left image and dark blue line shown in the right image of Fig. 5 (e).

Comparing the computer segmentation of CEP to manual drawing, mean Jaccard index for all 48 CEP samples was 0.7296 while mean Cohen's Kappa coefficient was 0.8286, showing a good agreement. The processing time for segmentation of one CEP was 0.59 s in average with Inter Core i7-2670QM (2.20 GHz). A manual segmentation of one CEP line would take 2 to 3 minutes.

The results of Pearson correlations showed that mean thicknesses of CEP lines (pink lines) in HE staining histological images were significant correlated with those of CEP lines segmented with the proposed method ($r=0.656$, $p=0.002$). Similar results were also observed between CEP lines (blue lines) in MT staining histological images and CEP lines segmented with the proposed method ($r = 0.834$, $p = 4.8\times10^{-6}$). The results of paired T tests showed that mean thicknesses of CEP lines (pink lines, 0.365 ± 0.041 mm) in HE staining images were significant smaller ($p = 0.002$) than those of CEP lines segmented with the proposed method (0.394 ± 0.046 mm); while, mean thicknesses of CEP lines (blue lines, 0.424 ± 0.065 mm) in MT staining images were significant larger ($p = 0.002$) than those of CEP lines segmented with the proposed method.

After segmentation of CEP in 3D, topographic maps of the outer and inner surfaces could be obtained to provide an intuitive view of CEP surface morphology (Fig. 6 (a)). Mean depths and cross sectional areas of 48 CEPs had been calculated, which were 1.288 ± 0.551 mm and 187.9736 ± 29.3113 mm^2 respectively. Then, thickness distribution map and UTE signal intensity distribution map as well as their corresponding histograms were obtained to provide an overall view of CEP thickness and UTE signal intensity, as is shown in Fig. 6 (b) and (c) respectively. Mean thickness value of 48 CEPs was 0.362 ± 0.037 mm.

The processing time for the whole procedure including CEP segmentation and CEP property measurements was 59.2 s with our methods (CPU: Inter Core i7-2670QM 2.20 GHz, RAM: 4 G); while, at least one hour was estimated to perform similar analysis manually by an experienced radiologist.

4. Discussion

In this study, an automatic CEP segmentation method has been developed for CEP property evaluation. It has several advantages over manual segmentation, including time saving, no subjective bias and global property evaluation. It will work better in CEP related studies, *e.g.*, to find out CEP defects and assess its integration.

Before the segmentation of CEP, the target IVD was identified by drawing a ROI in a sagittal UTE MRI image (Fig. 5(a)). ROI selection can greatly decrease interference of other tissues and make CEP lines clearer in the segmented block images, making it easier

for following segmentation procedure (Fig. 5 (a)). In the original block images, CEP lines are not smooth enough due to the limitation of current UTE MRI resolution. An up-sampling procedure can help increase image resolution and smooth the CEP lines. Compared with up-sampling algorithms performed in spatial domain, those processed in discrete cosine transform (DCT) domain usually has better performance and lower computational complexity. Hence, one of the most conventional algorithms based on DCT domain, i.e., zero-padding method, was used in this study [16, 17]. The segmented block images may have various intensity ranges, making it difficult for uniform parameter setting. That's why normalization procedure should be performed before segmentation. "Two-peak curve" is a strong feature of CEP lines in the block images after image preprocessing (Fig. 3). Based on this "two-peak curve", outer and inner borders of CEP lines can be easily identified (Fig. 5(b)), and corresponding CEP lines have been segmented with these borders.

The segmented CEP lines are very similar to those manually segmented by the experienced radiologist, as shown by the mean Jaccard index as well as mean Cohen's Kappa coefficient. But our processing time is much shorter than the manual segmentation. In addition, the segmented CEP lines have similar shape to the pink and blue lines in HE and MT staining images respectively (Fig. 5(e)), and the pink and blue lines have already been reported to correspond to CEP tissues [18, 19]. Pearson correlations in histological validation show that relative thickness change of CEP lines segmented with the proposed method is consistence with the actual change revealed by histological images. Interestingly, paired T tests show that CEP lines segmented with the proposed method are generally wider

than those revealed in HE staining images, but narrower than those revealed in MT staining images. That is because the HE staining only colors the eosinophilic structure (intracellular and extracelluar proteins) in the CEP pink, while the MT staining stains all the collagen fibers blue; the thickness of CEP observed by MT staining was hence larger than that observed by HE staining. Based on these findings, the proposed CEP segmentation method is a good replacement of conventional manual ones and the segmented CEP lines are enough to reflect some properties of CEP.

After assembling all segmented CEP lines, we can segment the entire CEP. Then 3D visualization of CEP can be achieved (Fig. 5 (d)), and some useful properties, *e.g.*, morphology, thickness and signal intensity, can also be presented in a global view to conduct more comprehensive evaluations of CEP status than those based on conventional 2D information.

CEP morphology is an indicator of its mechanical connection with neighboring tissues like IVD and bony endplate. The proposed method can provide a 3D visualization of its surface morphology (Fig. 6 (a)) and perform quantitative measurements, e.g., mean depth and cross sectional area, to make a better detection of morphology changes. Previously, this kind of global qualitative and quantitative assessments could only be conducted to *in-vitro* samples by a laser scanner [15]. The proposed method makes it possible in *in-vivo* studies.

CEP thickness was reported to have a relationship with CEP permeability, and its changes may reflect the variation of nutrition transportation to IVD [20, 21]. Based on the

histological validation, relative thickness change revealed with the proposed method is consistent with the actual change revealed in histological images. Furthermore, this method can generate a thickness distribution map, where global thickness change can be more easily detected. It is faster and clearer than most conventional thickness measurements, e.g., manual measurement of several positions along the CEP lines in mid-sagittal MRI image [7].

Abnormal signal intensities, e.g., focal loss and discontinuity, are direct indicators of CEP defects [8]. Conventionally, these abnormal patterns are usually observed by researchers on 2D MRI images, time consuming and easy to get wrong. The signal intensity distribution map (Fig. 6 (c)) generated with the proposed method can provide an easy and clear detection of abnormal signal intensities. Fig. 7 shows such an example. Four discontinuous points were created in four continuous sagittal UTE MRI images respectively (Fig. 7 (a)), as a simulation of the situation in [10]. With conventional method, we needed to observe every sagittal UTE MRI image and pick out all discontinuous points to declare a CEP defect; while with the proposed method, these four discontinuous points could be clearly revealed in the signal intensity distribution map (Fig. 7(b)).

What's more, the processing time for a comprehensive evaluation of CEP status with the proposed method is far shorter than those of other evaluations adopted in previous studies. It was counted that the processing time took less than one minute; while it would take an hour or more to achieve a similar measurement by an experienced researcher with conventional methods.

In this method, there is a ratio coefficient γ_i to control the width of CEP lines. This parameter can uniformly narrow or broaden the segmented CEP lines, but it won't change contour shapes of the CEP lines. The detailed adjustment procedure could be seen in Appendix C. The setting of this parameter is based on the understanding of CEP lines in UTE MRI images, and in this study it was set based on the consensus of the radiologist as well as several researchers experienced in CEP studies. This parameter can be adjusted if there is a different understanding of CEP lines, but it should be set uniformly for all CEP data involved in the same study.

There are some limitations in this study. The segmentation algorithm used in this study may not be reliable in detection of the CEP in the outer rim of the disc, which is adjacent to annulus fibrosus. Annulus fibrosus had shown similar signal intensities to those of CEP, making it very difficult to be discriminated from CEP in an UTE MRI image. Fortunately, in most cases we only focus on the central part of CEP because the nutrient diffusivities through the CEP, on which most of the disc cells are reliant, were region-dependent and occurred mainly in about 30% of the central part [3, 22, 23]. Another limitation is that the method cannot detect differences in cross sectional areas between the cranial and caudal CEPs of one target IVD. That is because cranial and caudal CEP lines corresponded to the two peaks respectively and would be segmented at the same time. Further study will be designed to solve these problems, e.g., to merge T1/T2 image as landmarks.

In addition, this study was carried out based on the donated goat's spines, which cannot

demonstrate the detection of abnormality. Further studies to explore the pathology of CEP diseases and other related diseases like IVD degeneration will be carried out and reported in the future.

5. Conclusions

To conclude, in this study a new technique to facilitate CEP evaluation based on UTE MRI scanning was developed. This technique offers an objective and efficient way for CEP segmentation and it is able to reveal several valuable properties of CEP, *e.g.*, morphology, thickness distribution and signal intensity distribution, comprehensively and with a good visualization presentation. Using this technique, both qualitative and quantitative evaluation of the CEP can be easily and accurately achieved.

Acknowledgments

This work was financially supported by the Research Grants Council of Hong Kong (773112) and the Tam Sai Kit Endowment Fund. We are very grateful to Mr Tong Tse from the 3T MRI Unit, the University of Hong Kong for technical support in MRI scanning, and Dr. Qian Wenshu from Department of Orthopaedics & Traumatology, Li Ka Shing Faculty of Medicine, the University of Hong Kong for manual CEP drawing.

References

[1] Y.C. Huang, V.Y. Leung, W.W. Lu, K.D. Luk, The effects of microenvironment in mesenchymal stem cell-based regeneration of intervertebral disc, Spine J, 13 (2013) 352-362.

[2] S.J. Ferguson, T. Steffen, Biomechanics of the aging spine, European Spine Journal, 12 (2003) S97-S103.

[3] Y.C. Huang, J.P. Urban, K.D. Luk, Intervertebral disc regeneration: do nutrients lead the way?, Nat Rev Rheumatol, 10 (2014) 561-566.

[4] W.C. Bae, S. Statum, Z. Zhang, T. Yamaguchi, T. Wolfson, A.C. Gamst, J. Du, G.M. Bydder, K. Masuda, C.B. Chung, Morphology of the cartilaginous endplates in human intervertebral disks with ultrashort echo time MR imaging, Radiology, 266 (2013) 564-574.

[5] M.D. Robson, P.D. Gatehouse, M. Bydder, G.M. Bydder, Magnetic resonance: an introduction to ultrashort TE (UTE) imaging, J Comput Assist Tomo, 27 (2003) 825-846.

[6] P. Gatehouse, G. Bydder, Magnetic resonance imaging of short T 2 components in tissue, Clin Radiol, 58 (2003) 1-19.

[7] S.M. Moon, J.H. Yoder, A.C. Wright, L.J. Smith, E.J. Vresilovic, D.M. Elliott, Evaluation of intervertebral disc cartilaginous endplate structure using magnetic resonance imaging, European Spine Journal, 22 (2013) 1820-1828.

[8] W. Bae, T. Yoshikawa, A. Hemmad, Ultrashort time-to-echo MRI of human intervertebral disc endplate: association with disc degeneration, Proc Int Soc Magn Reson Med, 2010, pp. 534.

[9] W. Bae, K. Xu, N. Inoue, G. Bydder, C. Chung, K. Masuda, Ultrashort time-to-echo MRI of human intervertebral disc endplate: association with endplate calcification, Proc

Int Soc Magn Reson Med, 2010, pp. 3218.

[10] T. Law, M.P. Anthony, Q. Chan, D. Samartzis, M. Kim, K.M. Cheung, P.L. Khong, Ultrashort time-to-echo MRI of the cartilaginous endplate: technique and association with intervertebral disc degeneration, J Med Imaging Radiat Oncol, 57 (2013) 427-434.

[11] V.E. Arpinar, S.D. Rand, A.P. Klein, D.J. Maiman, L.T. Muftuler, Changes in perfusion and diffusion in the endplate regions of degenerating intervertebral discs: a DCE-MRI study, European Spine Journal, (2015) 1-10.

[12] J. Xiao, Y.-C. Huang, S.K. Lam, K.D. Luk, Surgical technique for lumbar intervertebral disc transplantation in a goat model, European Spine Journal, 24 (2015) 1951-1958.

[13] S. Nielles‐Vallespin, M.A. Weber, M. Bock, A. Bongers, P. Speier, S.E. Combs, J. Wöhrle, F. Lehmann‐Horn, M. Essig, L.R. Schad, 3D radial projection technique with ultrashort echo times for sodium MRI: clinical applications in human brain and skeletal muscle, Magn Reson Med, 57 (2007) 74-81.

[14] Y. Wang, T. Videman, M.C. Battie, Morphometrics and lesions of vertebral end plates are associated with lumbar disc degeneration: evidence from cadaveric spines, J Bone Joint Surg Am, 95 (2013) e26.

[15] Y. Wang, M.C. Battié, T. Videman, A morphological study of lumbar vertebral endplates: radiographic, visual and digital measurements, European Spine Journal, 21 (2012) 2316-2323.

[16] J. Agbinya, Interpolation using the discrete cosine transform, Electron Lett, 28 (1992) 1927-1928.

[17] K.-W. Hung, W.-C. Siu, Novel DCT-Based Image Up-Sampling Using

Learning-Based Adaptive-NN MMSE Estimation, Circuits and Systems for Video Technology, IEEE Transactions on, 24 (2014) 2018-2033.

[18] K. Ariga, S. Miyamoto, T. Nakase, S.y. Okuda, W. Meng, K. Yonenobu, H. Yoshikawa, The relationship between apoptosis of endplate chondrocytes and aging and degeneration of the intervertebral disc, Spine, 26 (2001) 2414-2420.

[19] C.P. Paul, H.A. Zuiderbaan, B.Z. Doulabi, A.J. van der Veen, P.M. van de Ven, T.H. Smit, M.N. Helder, B.J. van Royen, M.G. Mullender, Simulated-physiological loading conditions preserve biological and mechanical properties of caprine lumbar intervertebral discs in ex vivo culture, (2012).

[20] F. Accadbled, J.-M. Laffosse, D. Ambard, A. Gomez-Brouchet, J.S. De Gauzy, P. Swider, Influence of location, fluid flow direction, and tissue maturity on the macroscopic permeability of vertebral end plates, Spine, 33 (2008) 612-619.

[21] A. Shirazi-Adl, M. Taheri, J. Urban, Analysis of cell viability in intervertebral disc: Effect of endplate permeability on cell population, J Biomech, 43 (2010) 1330-1336.

[22] Y. Wu, S.E. Cisewski, N. Wegner, S. Zhao, V.D. Pellegrini, E.H. Slate, H. Yao, Region and strain-dependent diffusivities of glucose and lactate in healthy human cartilage endplate, J Biomech, (2016).

[23] J. Urban, S. Holm, A. Maroudas, A. Nachemson, Nutrition of the Intervertebral Disk: An In Vivo Study of Solute Transport, Clinical orthopaedics and related research, 129 (1977) 101-114.

Figure legends

Fig. 1. Flowchart of cartilaginous endplate (CEP) segmentation and properties calculation based on UTE MRI data.

Fig. 2. Schematic diagram of CEP line segmentation. In the diagram, X represents the anterior-posterior direction, and Y represents the cranial-caudal direction. The blue curve represents signal intensities along Y direction at one specific position at X axis, as shown by the red line. The red line has two intersections with outer and inner borders of the CEP line respectively, i.e., outer border intersection and inner border intersection. Signal intensities of these two intersections are located at the outer and inner slopes of the two-peak curve's peak.

Fig. 3. Schematic diagrams of CEP properties calculation. (a) Schematic diagram of the inscribed sphere between outer surface and inner surface. (b) Schematic diagram of the projection from CEP surface to cross sectional plane.

Fig. 4. Schematic diagram of CEP line manual segmentation protocol. Manual segmentation was conducted in the central part of the block image. Borders of the CEP line were recognized as indicated by the black arrows.

Fig. 5. Results of image preprocessing and CEP segmentation. (a) Results of image preprocessing. The original sagittal UTE MRI image is shown in the left, where L2/3, L3/4, L4/5 and L5/6 denote different IVD positions and the selected ROI is marked by the red

box; the segmented block image is shown in the top right corner and the block image after up-sampling is shown in the bottom right corner. (b) Results of identification of inner and outer borders of CEP lines in a block image. The inner and outer borders are represented by the green and blue curves respectively, and the peaks' apexes are represented by the red curves. (c) Results of CEP lines segmentation. CEP lines are denoted by the green color. The upper one belongs to cranial CEP and the lower one belongs to caudal CEP. (d) 3D visualization of spine sample, sagittal section of sample, as well as cranial and caudal CEPs. (e) Histological image of CEP: HE (left) and MT (right), scale bar = 500 μm.

Fig. 6. Results of CEP properties calculation. (a) Topographic maps of outer (left) and inner (right) surfaces of the CEP. (b) Thickness distribution map (left) and its histogram (right). Color bar denotes thickness. (c) Signal intensity distribution map (left) and its histogram (right). Color bar denotes signal intensity.

Fig. 7. Comparison of CEP defects in sagittal UTE-MRI images and in signal intensity distribution map. (a) A simulation of CEP defects in four continuous sagittal UTE MRI images. (b) A simulation of CEP defects in signal intensity distribution map. Color bar denotes signal intensity.

Fig. A. 1. Schematic diagrams of automatic ROI selection and ROI shift estimation. (a) Schematic diagram of automatic ROI selection. "First slice", "Last slice" and "Middle slice" denote the first, last and middle slices of sagittal UTE MRI images respectively. "Start slice" and "End slice" denote the start and end slices of sagittal UTE MRI images that contain

CEP lines respectively. “Forward” denotes the direction from middle slice to first slice and “Backward” denotes the direction from middle slice to last slice. Reference ROI was first selected in the middle slice and then searched in forward and backward direction respectively. (b) Schematic diagram of ROI shift estimation. In the diagram, X represents the anterior-posterior direction, and Y represents the cranial-caudal direction. Δx and Δy represent shifts between target and reference ROIs in X and Y axes respectively.

Fig. B. 1. Schematic diagram of “two-peak curve” recognition. Y represents the cranial-caudal direction. The curve represents signal intensities along Y direction at one specific position in X axis, as the blue curve shown in Fig. 3. The “two-peak curve” is highlighted by the red color with its ascend and descend slopes, width, mean height, midpoint, as well as left and right peaks marked in the diagram. Apexes and feet of ascend and descend slopes are also marked in the diagram.

Fig. C. 1. Schematic diagram of border intersection targeting. Y represents the cranial-caudal direction. The intensity curve (blue curve) is the enlarged view of that in Fig. B. 1. Its gradient is represented by the intensity gradient curve (green curve). The red part of the intensity curve corresponds to CEP line determined by the outer and inner border intersections. $y_{apex,asc}$ is the position of ascend slope’s apex at Y axis. $y'_{out,asc}$ and $y'_{in,asc}$ are positions of initial outer and inner border intersections at Y axis. $y_{out,asc}$ and $y_{in,asc}$ are positions of the final outer and inner border intersections at Y axis. $d'_{out,asc}$ and $d'_{in,asc}$ are distances between the apex and initial outer as well as inner border intersections respectively. $d_{out,asc}$ and $d_{in,asc}$ are distances between the apex and outer as well as inner

1 border intersections respectively. γ_{asc} is a ratio between $d_{out,asc}$ and $d'_{out,asc}$. Subscript
2 “asc” means the border intersection targeting was performed in the ascend slope of the
3 “two-peak curve”. If this procedure is conducted in the descend slope, the subscript will be
4 changed into “des”.
5

Appendices

A. Automatic ROI selection

CEP was located in the central slices of sagittal UTE MRI images (Fig. A. 1(a)), and the positions of CEP lines in two neighboring slices were close to each other, only with a slight shift. Based on these facts, ROI selection could be performed automatically with the following steps:

(1) Select the middle slice (Fig. A. 1 (a)), as reference slice and select the ROI in reference slice manually as the reference ROI;
(2) Select the forward neighboring slice of the reference slice as target slice;
(3) Estimate shift of CEP line's positions in reference slice and target slice;
(4) Calculate ROI's position in target slice based on shift and reference ROI;
(5) Set target slice as the new reference slice and its ROI as the new reference ROI. Then, jump to step (2) unless the new reference slice was the first slice (Fig. A. 1(a)).

Steps (1)-(5) demonstrate a forward-direction searching. When it stopped at the first slice, ROIs in slices ahead of the middle slice had been selected; while, slices behind the middle slice had not been searched. Then we repeated steps (1)-(5) but to change "forward" to "backward" and "first slice" to "last slice" in step (2) and (5) respectively, *i.e.*, to conduct a backward-direction searching. For this time, there was no need for manual selection of the reference ROI in the middle slice in step (1); we just used the one selected at the beginning. After these two searching, ROIs in all slices had been found out and step (6) was then conducted.

(6) Draw ROIs in each slice and select the start and end slices containing CEP lines (Fig. A. 1 (a)). Reserve ROIs located between the start and end slices.

In step (3), shift was estimated by:

$$\left(\Delta x_t, \Delta y_t\right) = \arg\max_{\Delta x, \Delta y} S\left(\Delta x, \Delta y\right) \tag{A.1}$$

where $\left(\Delta x, \Delta y\right)$ denotes the shift between the reference ROI in the reference slice and the tested ROI in the target slice. $S\left(\Delta x, \Delta y\right)$ is a function to evaluate similarity between signal intensities in the reference and tested ROIs, calculated by:

$$S\left(\Delta x, \Delta y\right) = \sum_{x_r} \sum_{y_r} I_r\left(x_r, y_r\right) \oplus I_t\left(x_r + \Delta x, y_r + \Delta y\right) \tag{A.2}$$

where $I_r\left(x_r, y_r\right)$ denotes signal intensities of the reference ROI, and $I_t\left(x_r + \Delta x, y_r + \Delta y\right)$ denotes signal intensities of the tested ROI. The estimation step was illustrated in Fig. A. 1 (b).

B. "Two-peak curve" recognition

"Two-peak curve" recognition was one of the key processes of CEP line segmentation. In this study, the "two-peak curve" was recognized by examining its properties, such as ascend slope, descend slope, width, mean height and midpoint (Fig. B. 1). "Two-peak curve" was located in the curve representing signal intensities (Fig. 3); thus, its properties were calculated based on corresponding signal intensities.

Particularly, ascend and descend slopes were defined as outer slopes of left and right peaks

respectively. Their heights were calculated by:

$$\begin{cases} H_{slope,asc} = I\left(y_{apex,asc}\right) - I\left(y_{foot,asc}\right) \\ H_{slope,des} = I\left(y_{apex,des}\right) - I\left(y_{foot,des}\right) \end{cases} \quad \text{(B.1)}$$

where $y_{apex,i}$ and $y_{foot,i}$ represent Y axis positions of the apex and foot of slope *i* (i.e., "*asc*" denotes ascend slope or "*des*" denotes descend slope) respectively. $I\left(y\right)$ is the signal intensity at position y.

Width was defined as:

$$w = y_{mid,des} - y_{mid,asc} \quad \text{(B.2)}$$

where $y_{mid,i}$ represents Y axis position of middle point of slope *i* (i.e., "*asc*" denotes ascend slope or "*des*" denotes descend slope), calculated by:

$$\begin{cases} y_{mid,asc} = \left(y_{apex,asc} - y_{foot,asc}\right)/2 + y_{foot,asc} \\ y_{mid,des} = \left(y_{foot,des} - y_{apex,des}\right)/2 + y_{apex,des} \end{cases} \quad \text{(B.3)}$$

Mean height was defined as the mean value of signal intensities of the "two-peak curve" located between midpoints of ascend and descend slopes, calculated by:

$$\bar{H} = \bar{I}\left(y\right), y_{mid,asc} < y < y_{mid,des} \quad \text{(B.4)}$$

Midpoint of the "two-peak curve" was defined as the middle position of the "two-peak curve" located between midpoints of ascend and descend slopes, calculated by:

$$y_{mid,s} = \left(y_{mid,des} - y_{mid,asc}\right)/2 + y_{mid,asc} \quad \text{(B.5)}$$

With properties mentioned above, “two-peak curve” recognition process was performed as follows:

(1) Ascend and descend slopes with heights higher than the preset threshold (*i.e.*, 65 for data in this study) were selected. There might be more than one ascend slope as well as descend slope, forming more than one “two-peak curve”.

(2) “Two-peak curve” with width smaller than the preset threshold (*i.e.*, 5.9520 mm for data in this study) were removed.

(3) In the remaining “two-peak curves”, the one with the largest mean height was reserved as the right “two-peak curves”.

(4) In case of any false detection, midpoint position and width of a “two-peak curve” were used for further filtering. “Two-peak curves” were recognized at every position of X axis; nevertheless, target CEP lines existed only in the central part of X axis (Fig. 4). Thus, there was a need to remove false detected “two-peak curves” at two borders of X axis. As the right “two-peak curves” corresponded to the same IVD as well as its two neighboring CEPs, their midpoint positions and widths should form smooth curves along X direction. False detected “two-peak curves” could be picked out by checking sudden changes of these two curves. In this study, if the absolute value of a difference between two neighboring points was larger than 2.38 mm in midpoint position curve or 4.76 mm in width curve, it was treated as a sudden change.

C. Border intersection targeting

Border intersection targeting, another key process of CEP line segmentation, was a process to find outer and inner border intersections based on the recognized "two-peak curves". First, gradient of intensity of the "two-peak curve" was calculated by:

$$G(y)=\frac{dI(y)}{dy} \tag{C.1}$$

where y represents Y axis position and $I(y)$ represents signal intensity at position y.

Initial outer border intersection was targeted by finding the local maximum point of the gradient's absolute value, which was located on the outer slope of a peak and nearest to the apex. It was calculated by:

$$\begin{cases} f(y)=\left(\left|G(y)\right|-\left|G(y-1)\right|\right)\left(\left|G(y)\right|-\left|G(y+1)\right|\right) \\ y_{\max}=\arg\limits_{y} f(y)>0, \quad y\in\left(1,y_{apex,asc}\right) \text{ or } \mathrm{y}\in\left(\mathrm{y}_{apex,des},N_y\right) \\ y'_{out,i}=\arg\min\limits_{y_{\max}}\left|y_{\max}-y_{apex,i}\right|, \quad i=\text{"}asc\text{"} \text{ or } \text{"}des\text{"} \end{cases} \tag{C.2}$$

where $y_{\max}$ denotes the position of the local maximum point of gradient's absolute value. $y\in\left(1,y_{apex,asc}\right)$ or $\mathrm{y}\in\left(\mathrm{y}_{apex,des},N_y\right)$ indicated that this local maximum point should be located between the start point and the apex of the ascend slope (Fig. C. 1), or between the apex of the descend slope and the end point in the intensity curve. According to this rule, there might be two or more local maximum points, and the initial outer border intersection was picked out using the third formula, where subscript *i* represents ascend or descend slope when set as "asc" or "des" respectively.

Similar as initial outer border intersection, initial inner border intersection was defined as the local maximum point of the gradient's absolute value, which was located on the inner slope of a peak and nearest to the apex. It was calculated by:

$$\begin{cases} f(y) = \left(\left|G(y)\right| - \left|G(y-1)\right|\right)\left(\left|G(y)\right| - \left|G(y+1)\right|\right) \\ y_{\max} = \arg\limits_{y} f(y) > 0, \quad y \in \left(y_{apex,asc}, y_{apex,des}\right) \\ y'_{in,i} = \arg\min\limits_{y_{\max}} \left|y_{\max} - y_{apex,i}\right|, \quad i = "asc" \text{ or } "des" \end{cases} \tag{C.3}$$

where $y \in \left(y_{apex,asc}, y_{apex,des}\right)$ indicated that this local maximum point should be located between the apexes of the ascend and descend slopes (Fig. C. 1). The other settings were the same as those of formula (C.2).

Initial outer and inner border intersections were defined based on the conventional concept of edge in image processing; nevertheless, CEP line manually segmented by radiologist or revealed in histological images was usually narrower. Hence, a narrowing step was performed by scaling down the distances between border intersections and apexes, specifically as:

$$\begin{cases} y_{out,i} = y_{apex,i} + \mathrm{sgn}\left(y'_{out,i} - y_{apex,i}\right) \cdot d_{out,i} \\ y_{in,i} = y_{apex,i} + \mathrm{sgn}\left(y'_{in,i} - y_{apex,i}\right) \cdot d_{in,i} \end{cases}, \quad i = "asc" \text{ or } "des" \tag{C.4}$$

where $y_{out,i}$ and $y_{in,i}$ represent the final detected outer and inner border intersections, and sgn(y) was defined as:

$$\mathrm{sgn}(y) = \begin{cases} 1, & y > 0 \\ -1, & y < 0 \end{cases} \tag{C.5}$$

$d_{out,i}$ and $d_{in,i}$ represent distances between outer and inner border intersections and peak's

apex, specifically calculated by:

$$\begin{cases} d_{out,i} = \gamma_i \cdot d'_{out,i} \\ d_{in,i} = \gamma_i \cdot d'_{in,i} \end{cases}, \quad i = "asc" \text{ or } "des" \tag{C.6}$$

where γ_i is a ratio between 0 and 1, set as 0.75 in this study. $d'_{out,i}$ and $d'_{in,i}$ represent distances between initial outer and inner border intersections and peak's apex, specifically calculated by:

$$\begin{cases} d'_{out,i} = \left| y_{apex,i} - y'_{out,i} \right| \\ d'_{in,i} = \left| y_{apex,i} - y'_{in,i} \right| \end{cases}, \quad i = "asc" \text{ or } "des" \tag{C.7}$$

Subscript i in formula (C.4) to (C.7) represents ascend or descend slopes when set as "asc" or "des" respectively.

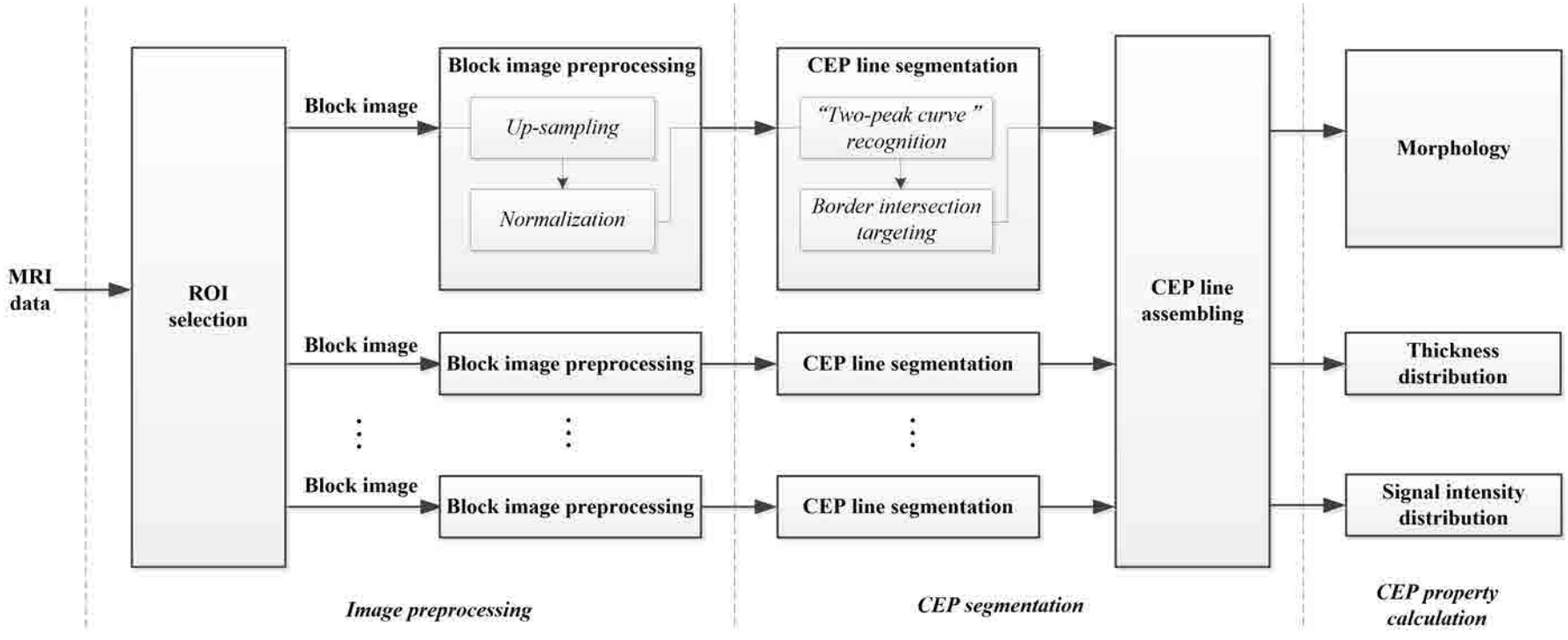
MRI data
ROI selection
Block image
Block image preprocessing
Up-sampling
Normalization
Block image
Block image preprocessing
Block image
Block image preprocessing
CEP line segmentation
"Two-peak curve" recognition
Border intersection targeting
CEP line segmentation
CEP line segmentation
CEP line assembling
Morphology
Thickness distribution
Signal intensity distribution
Image preprocessing
CEP segmentation
CEP property calculation

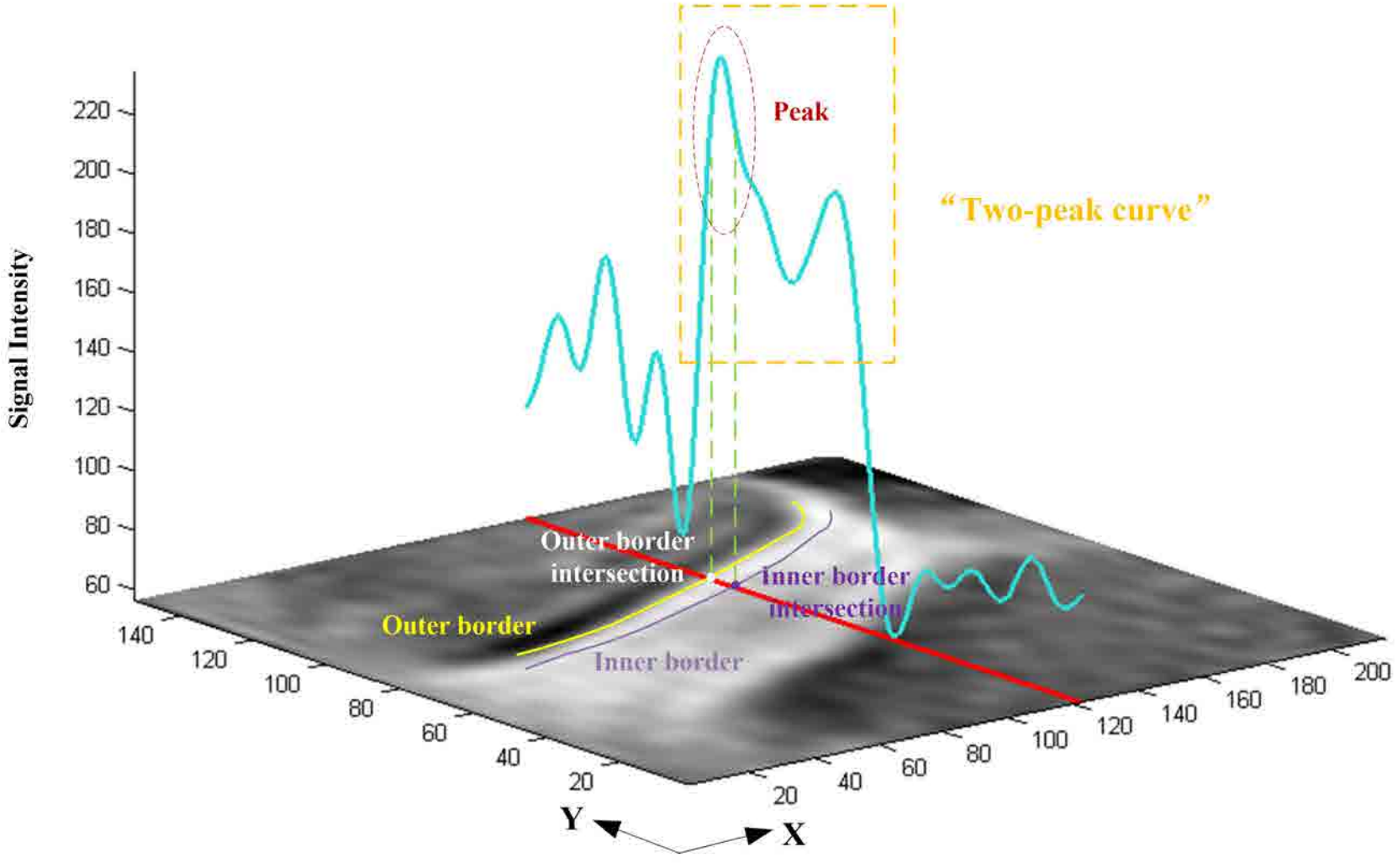
Signal Intensity
220
200
180
160
140
120
100
80
60
Peak
"Two-peak curve"
Outer border intersection
Inner border intersection
Outer border
Inner border
140
120
100
80
60
40
20
Y
20
40
60
80
100
120
140
160
180
200
X

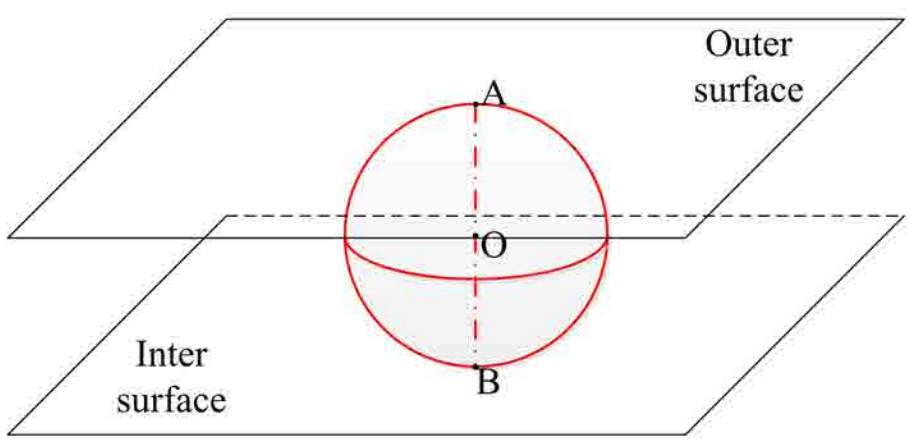
Outer
surface
A
O
Inter
surface
B

(a)

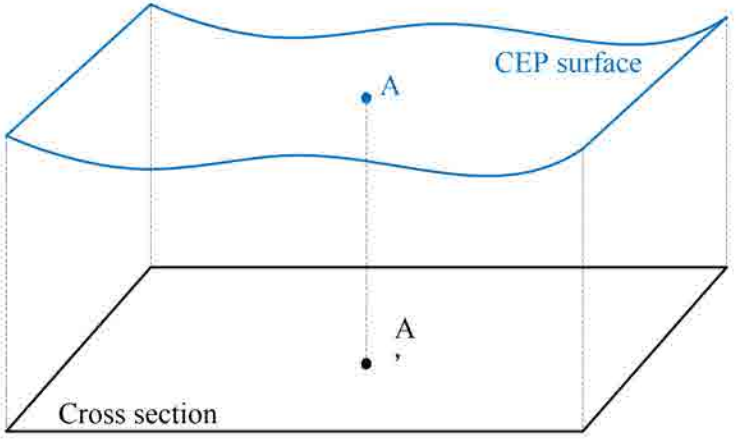
CEP surface
A
A
,
Cross section

(b)

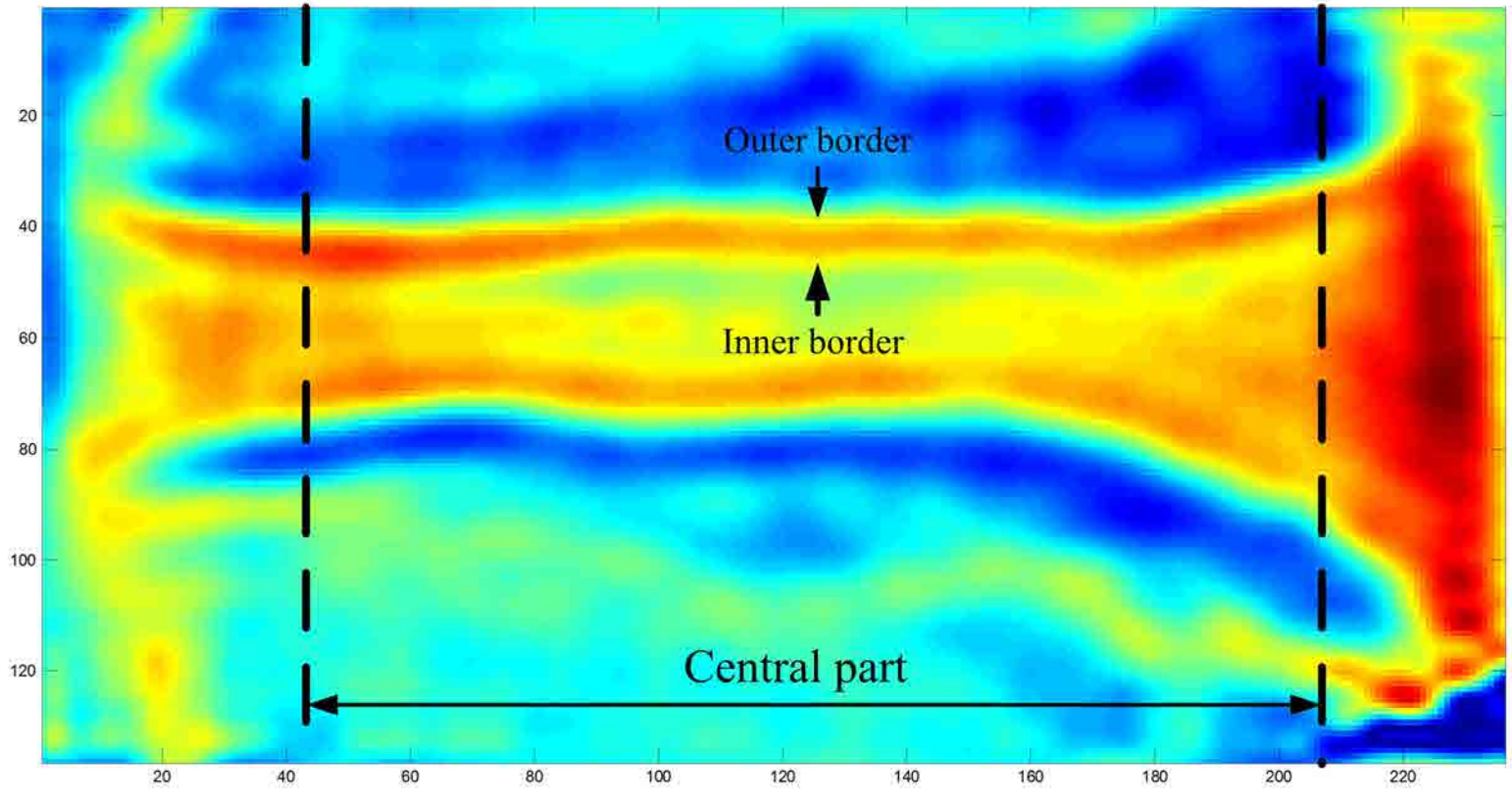
Outer border
Inner border
Central part
20
40
60
80
100
120
20
40
60
80
100
120
140
160
180
200
220

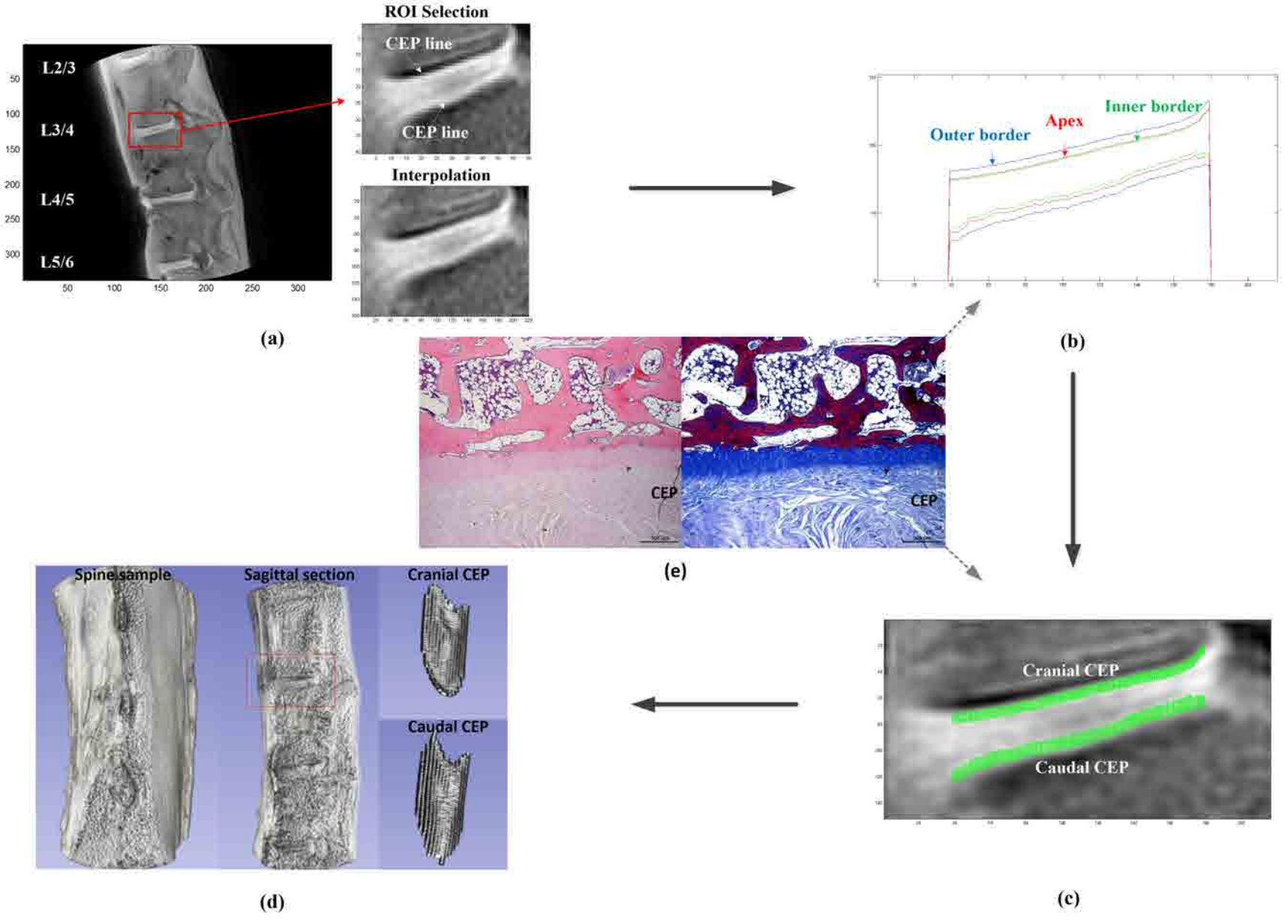
L2/3
L3/4
L4/5
L5/6
ROI Selection
CEP line
CEP line
Interpolation
(a)
Outer border
Apex
Inner border
(b)
CEP
CEP
(e)
Cranial CEP
Caudal CEP
(c)
Spine sample
Sagittal section
Cranial CEP
Caudal CEP
(d)

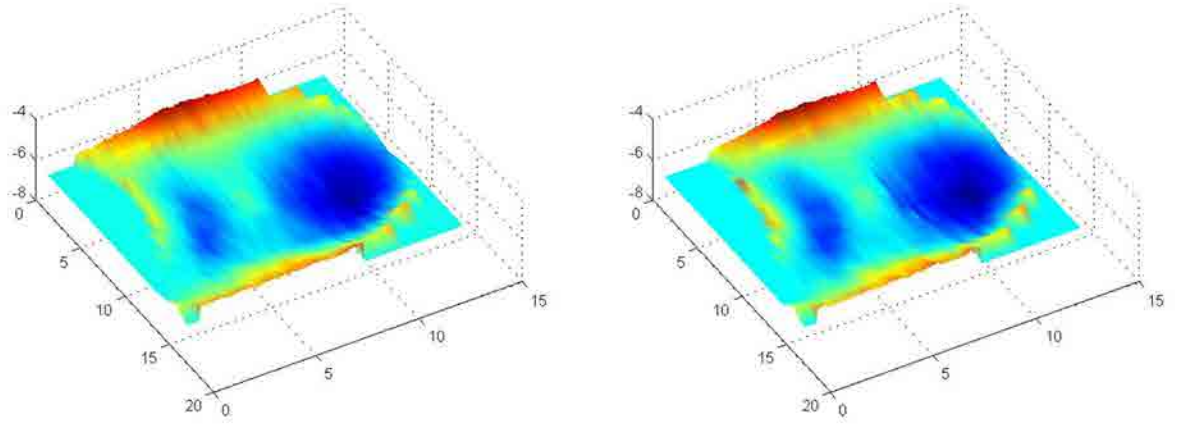
-4
-6
-8
0
5
10
15
20
0
5
10
15

(a)

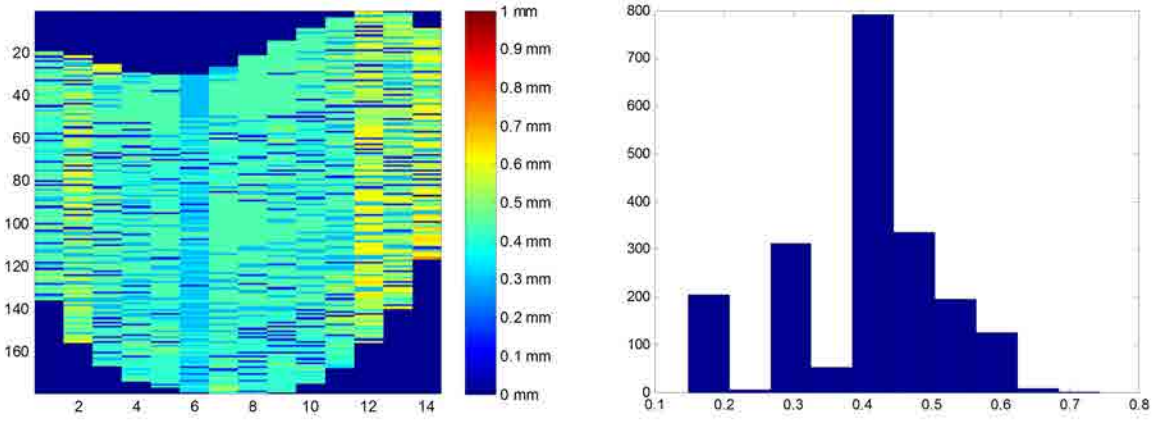
20
40
60
80
100
120
140
160
2
4
6
8
10
12
14
1 mm
0.9 mm
0.8 mm
0.7 mm
0.6 mm
0.5 mm
0.4 mm
0.3 mm
0.2 mm
0.1 mm
0 mm
800
700
600
500
400
300
200
100
0
0.1
0.2
0.3
0.4
0.5
0.6
0.7
0.8

(b)

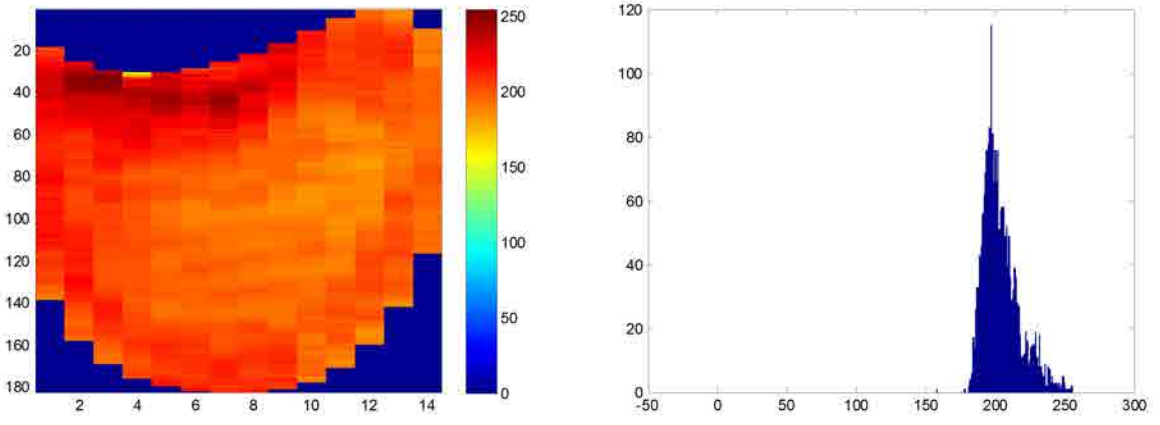
20
40
60
80
100
120
140
160
180
2
4
6
8
10
12
14
250
200
150
100
50
0
120
100
80
60
40
20
0
-50
0
50
100
150
200
250
300

(c)

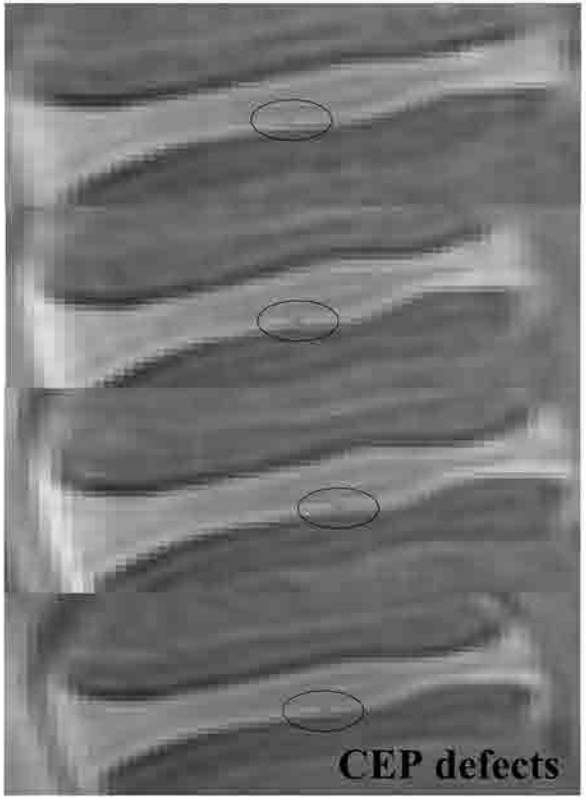
CEP defects

(a)

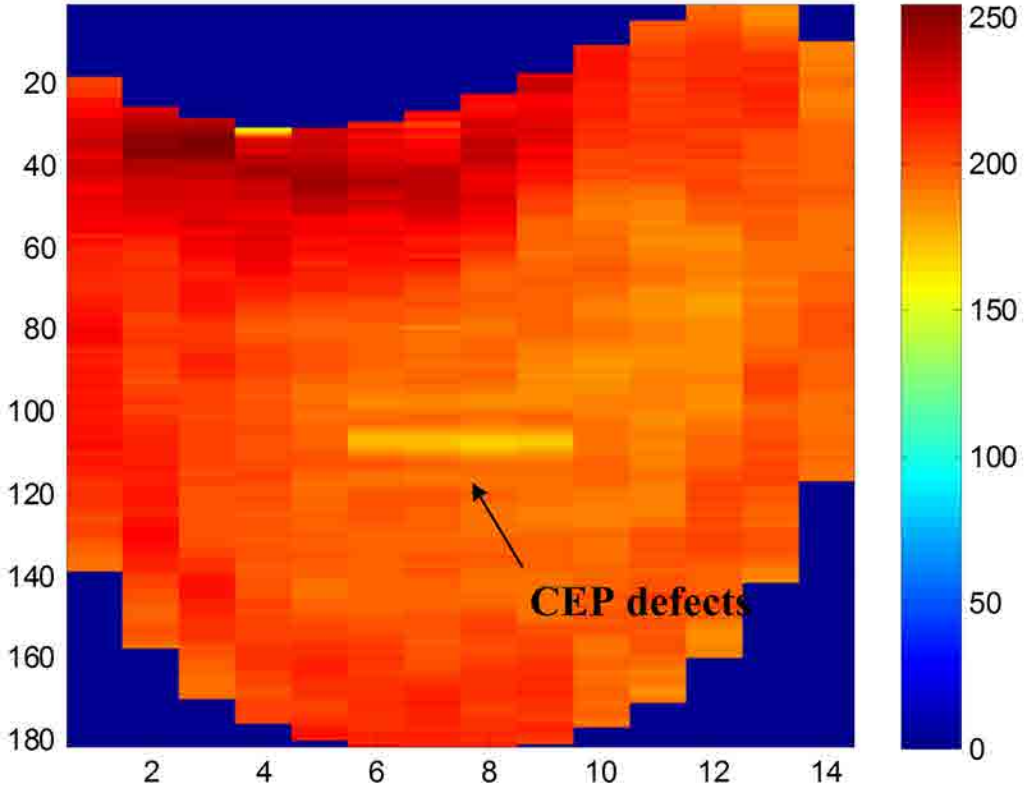
20
40
60
80
100
120
140
160
180
2
4
6
8
10
12
14
250
200
150
100
50
0
CEP defects

(b)

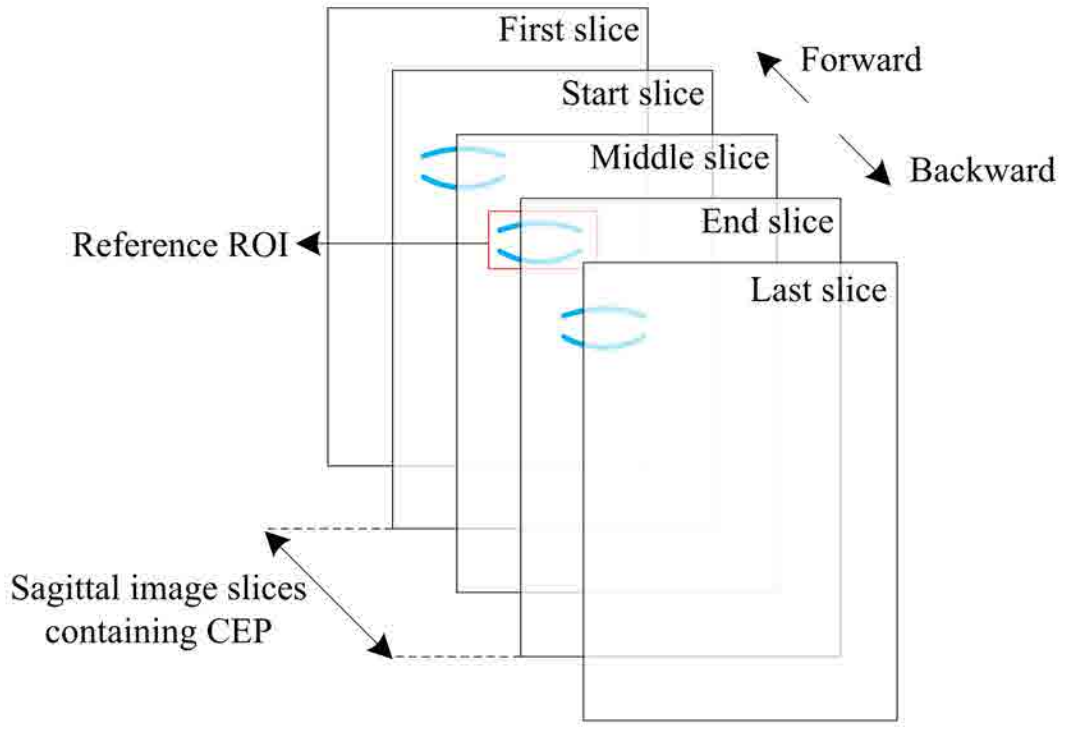
First slice
Start slice
Middle slice
End slice
Last slice
Forward
Backward
Reference ROI
Sagittal image slices
containing CEP

(a)

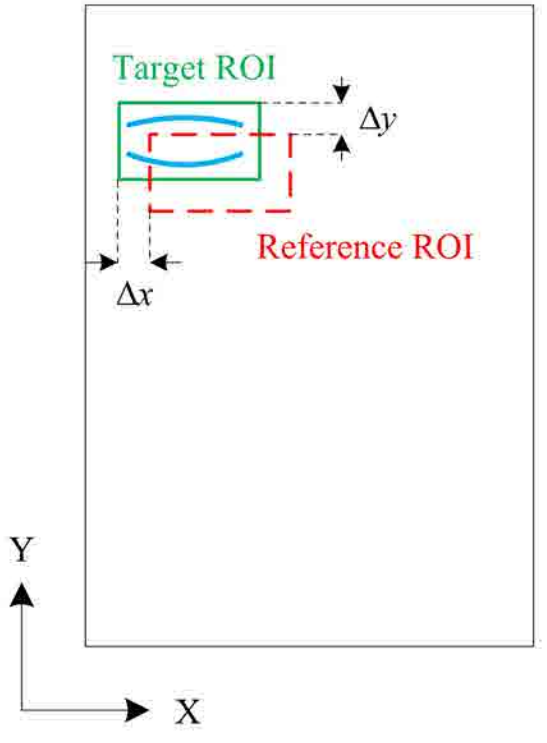
Target ROI
Δy
Reference ROI
Δx
Y
X

(b)

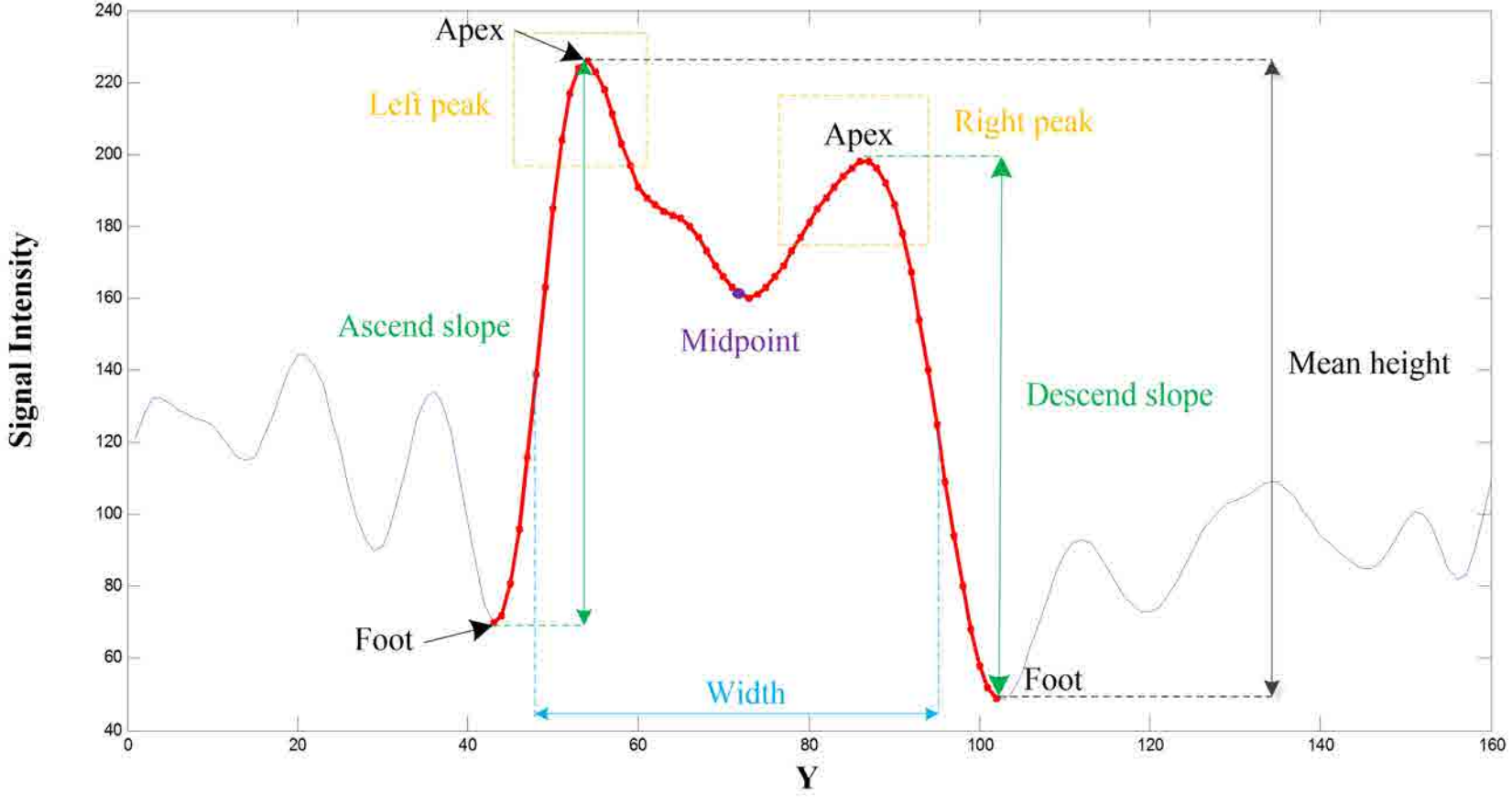
Apex
Left peak
Apex
Right peak
Ascend slope
Midpoint
Mean height
Descend slope
Foot
Foot
Width
Signal Intensity
Y
240
220
200
180
160
140
120
100
80
60
40
0
20
40
60
80
100
120
140
160

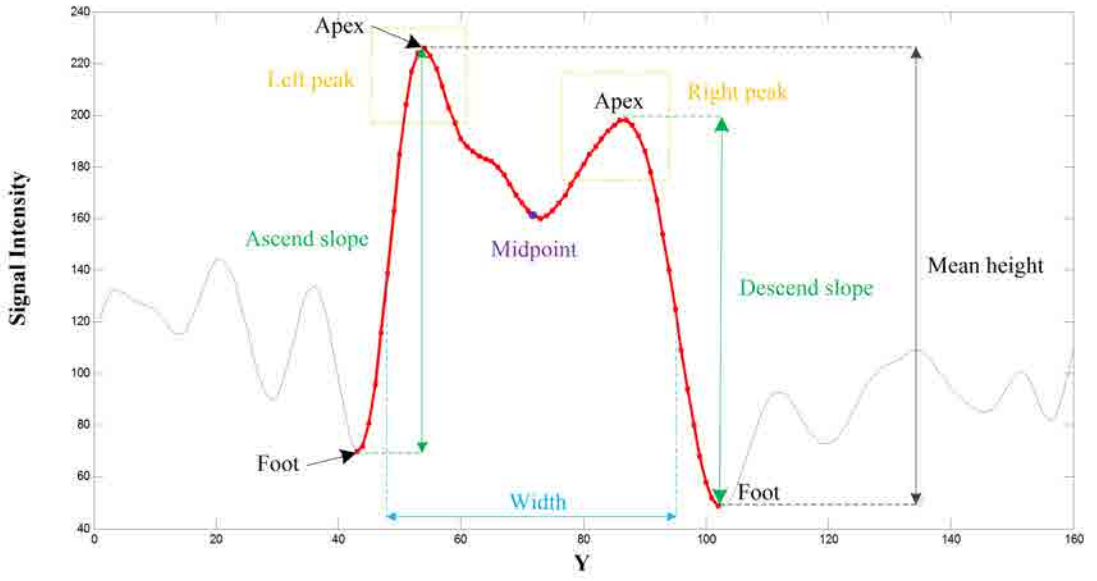
Apex
Left peak
Apex
Right peak
Ascend slope
Midpoint
Descend slope
Mean height
Foot
Width
Foot
Signal Intensity
Y

(a)

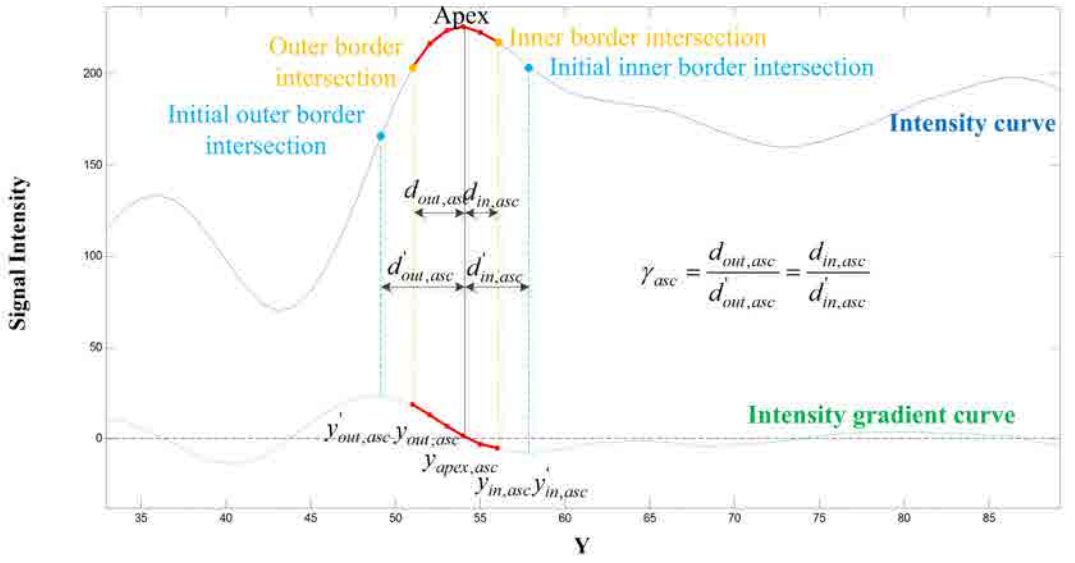
Apex
Outer border intersection
Inner border intersection
Initial inner border intersection
Initial outer border intersection
Intensity curve
$d_{out,asc}$ $d_{in,asc}$
$d'_{out,asc}$ $d'_{in,asc}$
$\gamma_{asc} = \frac{d_{out,asc}}{d'_{out,asc}} = \frac{d_{in,asc}}{d'_{in,asc}}$
Intensity gradient curve
$y'_{out,asc}$ $y_{out,asc}$
$y_{apex,asc}$
$y_{in,asc}$ $y'_{in,asc}$
Signal Intensity
Y

(b)